Nano Research

ISSN 1998-0124 CN 11-5974/O4
https://doi.org/10.1007/s12274-020-2662-7

Research Article

Multiaxially-stretchable kirigami-patterned mesh design for graphene sensor devices

Hyo Chan Lee[1,§], Ezekiel Y. Hsieh[1,§], Keong Yong[1], and SungWoo Nam[1,2,3,4,5] (✉)

[1] *Department of Mechanical Science and Engineering, University of Illinois at Urbana – Champaign, Urbana, Illinois 61801, USA*
[2] *Department of Materials Science and Engineering, University of Illinois at Urbana – Champaign, Urbana, Illinois 61801, USA*
[3] *Materials Research Laboratory, University of Illinois at Urbana – Champaign, Urbana, Illinois 61801, USA*
[4] *Micro and Nanotechnology Laboratory, University of Illinois at Urbana – Champaign, Urbana, Illinois 61801, USA*
[5] *Carle Illinois College of Medicine, University of Illinois at Urbana – Champaign, Champaign, Illinois 61820, USA*
[§] *Hyo Chan Lee and Ezekiel Y. Hsieh contributed equally to this work.*

Received: 6 November 2019 / **Revised:** 21 December 2019 / **Accepted:** 14 January 2020

ABSTRACT

In wearable electronics, significant research has gone into imparting stretchability and flexibility to otherwise rigid electronic components while maintaining their electrical properties. Thus far, this has been achieved through various geometric modifications of the rigid conductive components themselves, such as with microcracked, buckled, or planar meander structures. Additionally, strategic placement of these resulting components within the overall devices, such as embedding them at the neutral plane, has been found to further enhance mechanical stability under deformation. However, these strategies are still limited in performance, failing to achieve fully strain-insensitive electrical performance under biaxial stretching, twisting, and mixed strain states. Here, we developed a new platform for wearable, motion artifact-free sensors using a graphene-based multiaxially stretchable kirigami-patterned mesh structure. The normalized resistance change of the electrodes and graphene embedded in the structure is smaller than 0.5% and 0.23% under 180° torsion and 100% biaxial strain, respectively. Moreover, the resistance change is limited to 5% under repeated stretching–releasing cycles from 0% to 100% biaxial strain. In addition, we investigated the deformation mechanisms of the structure with finite element analysis. Based on the simulation results, we derived a dimensionless geometric parameter that enables prediction of stretchability of the structure with high accuracy. Lastly, as a proof-of-concept, we demonstrated a biaxially-stretchable graphene-based sensor array capable of monitoring of temperature and glucose level with minimized motion-artifacts.

KEYWORDS

kirigami, mesh, strain-insensitive, wearable, graphene, glucose

1 Introduction

Wearable sensors have the potential to enable real-time monitoring of an individual's state of health or remote diagnosis of diseases simply via attachment to the skin. To achieve this goal, a wide variety of wearable sensors capable of continuous bio-signal monitoring have been developed and investigated [1–4]. When developing such wearable sensors, user movement must be taken into account because body movements are normally accompanied by stretching or contraction of the skin [5]. This can cause deformation of the active sensing element or even delamination of the active sensing element from the skin [6], which will severely distort the output bio-signals. To avoid this susceptibility to motion artifacts, the components in wearable devices must be reversibly stretchable up to > 30% without change in their electrical properties, and they should fully adhere to the skin under body movements [7]. This task has been commonly accomplished by fabricating sensors on deformable planar substrates that adhere to the skin [8]. In particular, island–bridge configurations have been widely adopted using deformable planar substrates to achieve high stretchability for electronic components. In an island–bridge configuration, rigid sensing components (islands) are separated and joined by stretchable metal interconnects (bridges). Any overall strains become delocalized from the rigid islands, instead deforming the stretchable interconnect bridges, thereby minimizing the strain experienced by the sensing components. Despite significant progress in developing wearable sensors with this strategy, the stretchable planar substrates used can be problematic due to their limited softness [9]. Additionally, stretchable planar substrates are inherently not breathable, inhibiting gas permeation and potentially causing severe skin irritation after prolonged use [10].

Another promising platform for motion artifact-free wearable devices is mesh electronic structures [11, 12]. Porous mesh structures are highly deformable, even enabling syringe injectable mesh electronics to reach targeted internal cavities before unfolding into their fully expanded state [13]. In addition, thin mesh structures can ensure conformal contact to complex curvilinear surfaces [14]. The breathability of porous mesh structures is significantly better than that of stretchable planar substrates. Furthermore, multi-sensor devices can be fabricated using mesh structures by means of island–bridge concepts [15].

As a potential strategy for making highly stretchable mesh

Address correspondence to swnam@illinois.edu

structures, kirigami techniques have attracted much attention. Kirigami, a subgenre of the better-known origami (paper folding), involves the creation of three-dimensional (3D) structures through strategic incisions of two-dimensional (2D) sheets [16–20]. Thin films with kirigami patterns have out-of-plane deformation responses to elongation, redistributing in-plane stress into out-of-plane deformations under stretching, thereby providing macroscopic deformability of materials beyond their intrinsic mechanical properties. However, previously reported kirigami-based devices [21–23] were designed primarily for uniaxial stretching, only maintaining electrical properties under some specific mechanical deformations. Additionally, these devices were simple in functionality, with only one type of sensor, and therefore capable of only measuring a single signal.

Atomically thin materials offer unique advantages for wearable sensor applications, with enhanced electronic and functional properties over their bulk counterparts and readily tunable structures [24, 25]. In particular, graphene, an atomically-thin layer of carbon atoms, is mechanically robust [26], electrochemically stable [4], and biocompatible [27], which makes it a promising material for flexible or wearable sensors [28, 29]. Recently, we have developed wearable graphene kirigami-based devices capable of withstanding high uniaxial strains (up to 240%) [30]. Here, we improved upon our previous kirigami design by expanding it to a strain-insensitive, biaxially-stretchable, graphene-based sensor array. To this end, we combined kirigami techniques with the concept of island–bridge mesh electronics. The electrodes embedded in the kirigami-patterned mesh structure exhibit nearly constant electrical resistance under biaxial stretching of 100% and torsion of 180°. Moreover, the resistance change is limited to 5% under repeated stretching–releasing cycles from 0% to 100%. We additionally investigated the deformation mechanisms of the kirigami structure using finite element analysis (FEA) and proposed a simple dimensionless geometric parameter that can predict the overall stretchability of our kirigami or similar structures. Furthermore, we demonstrated strain-insensitive temperature sensing, and solution-gated graphene field-effect-transistor (GFET)-based glucose sensing using these devices.

2 Experimental

2.1 Fabrication of kirigami-patterned mesh sensors

The fabrication scheme is shown in Fig. S1 in the Electronic Supplementary (ESM). First, a sacrificial layer (150 nm-thick copper film) was deposited onto a Si wafer via electron beam evaporation. The bottom polyimide layer was spin-coated and then cured at 350 °C for 4 h under low pressure nitrogen flow. Graphene grown by chemical vapor deposition on copper foil (Fig. S2 in the ESM) was used for the GFET glucose sensors. After transferring graphene onto the bottom polyimide layer and annealing under argon flow, the graphene channels were patterned via photolithography and reactive ion etching (RIE). Next, Cr/Au/Ti metal electrodes (15/150/15 nm), including the contact pads and planar gates, were deposited. Additionally, an RIE etch stop (40 nm thick copper film) to protect the graphene channels was deposited before the top polyimide layer was spin-coated and cured. A 40 nm thick copper etch mask was then patterned on the top polyimide layer and the entire sandwich structure was then etched by RIE to create the kirigami cuts entirely through the polyimide. Finally, the device was released from the wafer by electroetching of the sacrificial layer, protective layer, and etch mask. The released device consists of a sandwich structure containing the electrodes and graphene between two polyimide layers with selective holes in the top layer enabling electrical contact to the graphene channels and contact electrodes. Polyimide was specifically chosen as the structural material for our design as it is biocompatible, readily spincoat-able, and highly inert to the chemicals and high temperatures involved in the photolithography process.

2.2 Finite element analysis of kirigami-patterned mesh structures

Non-linear finite element analysis was carried out using the Structural Mechanics Module in COMSOL Multiphysics®. For the polyimide structural material of the kirigami devices, we assumed a true stress–strain curve of the material as follows

$$\begin{aligned} \sigma &= E_1\varepsilon && \text{if } \sigma \le \sigma_y \\ \sigma &= E_2(\varepsilon - \varepsilon_y) && \text{if } \sigma > \sigma_y \end{aligned} \quad (1)$$

where E_1 is 2.1 GPa, E_2 is 214 MPa, σ_y is 144 MPa and ε_y is the strain where $E_1\varepsilon = \sigma_y$ [30]. The loading was imposed either by moving the ends along the plane in steps or directly applying axial forces to the ends. The increments of displacement or axial force were kept small for convergence of the non-linear problem.

3 Results and discussion

3.1 Design of kirigami-patterned mesh structure for strain-insensitive devices

Figures 1(a) and 1(b) show the overall structural design of our kirigami devices for strain-insensitive wearable sensing. We adopted a 2 × 2 island–bridge mesh structure with four separate islands, enabling multifunctional sensing (e.g., glucose, temperature) on the same device (Fig. 1(a)). The four islands are connected to each other and the outer contact pads with bridges. The island-to-contact pad bridges carry electrodes, while the island-to-island bridges do not. Figure 1(b) shows the final design of our kirigami devices (see also Fig. S3(a) in the ESM). To impose stretchability and enhance the breathability of the

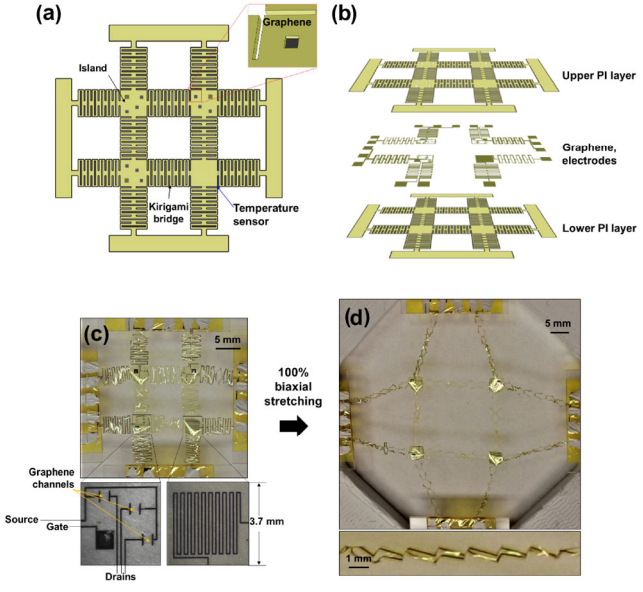

Figure 1 (a) Schematic illustration of strain-insensitive glucose sensor device fabricated in a kirigami-patterned mesh structure. (b) Graphene sensing channels and metal electrodes are embedded in polyimide. Photographs of the kirigami-patterned stretchable sensor in (c) neutral state and (d) 100% biaxially stretched state. Insets in (c) show photographs of graphene transistor (left) and temperature sensor (right) fabricated on islands, respectively. Lower image in (d) shows side-view out-of-plane deformation of a kirigami bridge.

mesh structure, kirigami cuts and notches were added to the bridges. On the islands, temperature and GFET glucose sensors were fabricated. As shown in Fig. 1(b), all of the electronic components are sandwiched at the neutral plane of the kirigami-patterned mesh structure. The thickness of the top and the bottom polyimide layers was 3–5 μm (Fig. S3(b) in the ESM). Small windows in the top layer of polyimide allow for electrolyte solution gating between the gates and graphene channels of the GFET-based glucose sensors.

Figures 1(c) and 1(d) show a graphene-based kirigami-patterned multi-sensor device in an unstretched (ε_n = 0%) and biaxially stretched (ε_n = 100%) state, respectively. Similar to previously reported kirigami structures with stretchable conducting electrodes [30], stretching of the overall structure causes out-of-plane deformations of the kirgami bridges. However, the additional 4-fold rotational symmetry of our kirigami structure allows it to stretch under biaxial loading.

In order to achieve motion artifact-free sensing for wearable devices, the most important requirement is that the electrical responses of electrodes and sensing electronics remain unchanged under various deformation conditions. Therefore, we assessed the normalized change in resistance ($\Delta R/R_0$) of the electrodes and graphene-based FET sensors embedded in our kirigami structure (Fig. 2). As the kirigami was twisted by applying torsional stress at the left and right ends (with the top and bottom ends fixed), there was a negligibly small change in resistance (< 0.5%) under torsional deformation (Fig. 2(a)). Similarly, stable electrical resistance was observed under biaxial stretching, with a change in resistance smaller than 0.3% for biaxial strain from ε_n = 0% to ε_n = 100% (Fig. 2(b) and Movie ESM1). The estimated strain gauge factor, defined as $\Delta R/R_0/\varepsilon_n$ was less than 6×10^{-4} for biaxial stretching. For both torsional biaxial strains, the mechanical responses of the fabricated kirigami-patterend devices matched well with the FEA simulations. We also carried out time-resolved current measurements for the electrode embedded in a kirigami structure while stretching it biaxially from 0% to 100%. The current remained stable over time, which demonstrates stability during movement (Fig. 2(c)).

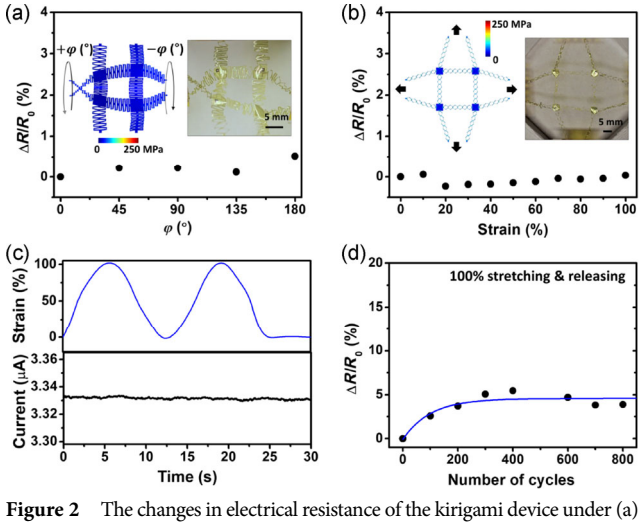

Figure 2 The changes in electrical resistance of the kirigami device under (a) twist angle (φ) up to 180°, (b) biaxial strain up to 100%. Inset images in (a) and (b) are von Mises stress distribution simulated by FEA and photographs of the kirigami-patterned device at φ = 90° (viewed at a slightly tilted angle from vertical) and ε_n = 100%, respectively. (c) Time-resolved current of the kirigami device under dynamic stretching conditions. The device was biaxially stretched in two consecutive cycles from ε = 0% to ε =100%. The stretching was initiated at time 0 s. (d) Changes in electrical resistance of the kirigami device under cyclic biaxial stretching between 0% and 100% up to 800 cycles.

Another important feature for wearable sensors is cyclic reversibility, as human skin is repeatedly stretched and contracted. In order to demonstrate reversibility and durability, the normalized resistance change was measured under repeated biaxial stretching–releasing cycles between ε_n = 0% and ε_n = 100% (Fig. 2(d)). Although there was an approximately 3.7% initial increase of resistance in the first 200 cycles, the normalized resistance stabilized and the resistance change was less than 2% between 200 and 800 stretching–releasing cycles. We attribute the small changes in resistance to unintentional overstretching (> 100%) of the kirigami structure during stretching–releasing cycles.

3.2 Finite element analysis and mechanics model of kirigami-patterned mesh structure

In order to understand the deformation mechanisms of our kirigami structure, we first characterized the mechanical response of a 10 μm-thick kirigami structure under biaxial loading using FEA (Fig. 3(a), see also Section 2). The simulated nominal stress–nominal strain (σ_n–ε_n) responses of the kirigami show three different stages (Fig. 3(b)). In stage I ($0 \le \sigma_n \le 0.125$ MPa, $0\% \le \varepsilon_n \le 0.25\%$), σ_n and ε_n have a linear relationship with the slope of 50 MPa. In this stage, the main deformation mechanism of the kirigami structure is in-plane bending of the bridges (see also Fig. S4 in the ESM). Next, in stage II ($0.125 \le \sigma_n \le 10$ MPa, $0.25\% \le \varepsilon_n \le 105\%$), the average tangent modulus drops significantly to 5.1 MPa as a result of the out-of-plane deformation of the bridges. As ε_n increases above 105% (stage III), the kirigami becomes rapidly stiffer. The slope at ε_n = 140% is 220 MPa, which is similar to the modulus of polyimide above its yield point (214 MPa).

On the islands, the average strain does not exceed 0.4% over the entire simulated range of σ_n (Fig. 3(c)), indicating that our kirigami design effectively distributes the stress away from the islands. Strain in the islands was estimated to be very limited under torsion of the overall device as well (Fig. S5 in the ESM).

The mechanical deformation of the kirigami bridges in stages II and III was further analyzed by dividing the unit cell of bridges into three plates. The unit cell of kirigami bridges consists of two long plates (P1), two connection plates at the cuts (P2) and one connection plate at the notch (P3) (Fig. 3(d)). Figure 3(e) shows the von Mises stress distribution in a kirigami bridge and its deformed structure at σ_n = 10 and 50 MPa. The stress was localized near the tip of cuts (see also Fig. S6 in the ESM). Under in-plane loading, the bending of P1 with out-of-plane rotation was predicted (Fig. 3(e)), which is consistent with our experimental observations (lower image of Fig. 1(d)). Owing to the out-of-plane bending of P1, the kirigami structure can be elongated in the in-plane direction significantly with a relatively small loading force. In stage II, the rotation angle (θ) of P1 plates gradually increases and then saturates at 76° (Fig. S7 in the ESM). The rotation of P1 accompanied by the torsion of P2 and rotation of P3 rather than stretching of P2 or P3 in stage II, results in a low effective modulus for the whole structure. After θ reaches to the saturation value, the main deformation mechanism of the kirigami structure transitions to stretching around P2 and P3 (stage III). Therefore, the in-plane stress starts to concentrate around P2 and P3 in stage III, and the effective modulus of the kirigami structure becomes similar to the modulus of polyimide. It is expected that mechanical failure of kirigami structures can easily take place when it is in stage III.

Next, 10 μm thick kirigami designs with varying design parameters g (including W, BW, CW, H, BH, CH) shown in Fig. 3(d) were also evaluated to explore the relationship between

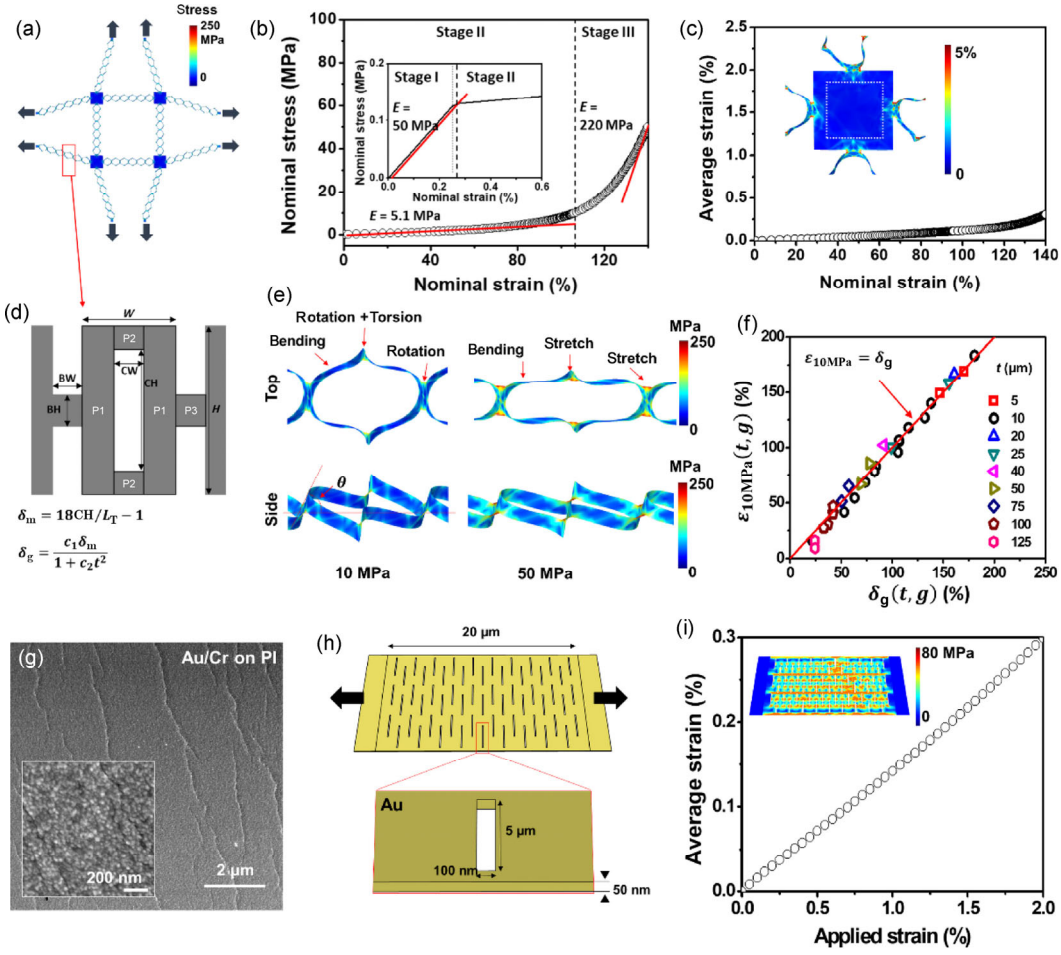

Figure 3 (a) Top view of entire kirigami structure and von Mises stress distribution in the structure under biaxial nominal stress of 10 MPa (or biaxial nominal strain of 105%). (b) Nominal stress–nominal strain curve of the kirigami structure. Inset shows the magnified plot for very small strains (ε_n < 0.6%). (c) Average principal strain in the island as a function of nominal strain. Inset shows strain distribution in the island under biaxial nominal stress of 10 MPa. (d) Schematic diagram of the unit cell of bridges and various geometric parameters. The unit cell consists of two P1 plates, two P2 plates and one P3 plate. (e) Top view and side view of the unit cell structure and stress distribution in the structure under nominal stress of 10 MPa (left) and 50 MPa (right). The thickness of kirigami structures in (a)–(e) is 10 μm. (f) The correlation between FEA-simulated ($\varepsilon_{10MPa}(t,g)$) and analytically calculated (δ_g) nominal strain of kirigami structures at nominal stress of 10 MPa. (g) Multiple microcracks and nanocracks (inset) formed in Au/Cr thin film deposited on the kirigami structure after stretching up to 100%. (h) FEA simulation of stress distribution in Au thin film (50 nm) with initial cracks. (i) FEA simulation of average strain in the Au thin film as a function of applied strain on the film.

the stretchability of kirigami designs and their design parameters (see also Fig. S8 in the ESM). CW and BH, which are not related to initial total length of the kirigami structure (L_T (μm) = 18W + 21 BW + 2H + 1000), barely affect the mechanical response of the kirigami structure (Figs. S8(b) and S8(c) in the ESM). On the other hand, the increase of CH allows for more elongation of the kirigami structure (Fig. S8(d) in the ESM). In addition, increasing either BW or W, which increases L_T, reduces the stretchability of the kirigami structure (Figs. S8(e) and S8(f) in the ESM). This parametric study clearly gives an insight into the effects of geometric parameters on the stretchability of the kirigami; the bendability of the P1 plate, which is proportional to CH, determines the overall stretchability of kirigami structure.

Our finding on how CH is related to kirigami stretchability is supported by following explanations. Assuming P1 can be completely folded with out-of-plane rotation of 90° and the bending of P1 plates is the only deformation mechanism, the total length of the kirigami structure after complete bending of P1 plates would be approximately 18 × CH. Nominal nominal strain in this case can be approximated as $\delta_m(g)$ = 18CH/L_T − 1. Next, we compare δ_m with the nominal strain of a 10 μm-thick kirigami structure at a nominal stress of 10 MPa (i.e., ε_{10MPa}(10 μm,g)). Here, 10 MPa was chosen because at that stress, kirigami structures will be in stage II or early stage III, with large deformations but minimized mechanical failure. We found that ε_{10MPa}(10 μm,g) and δ_m have a strong linear correlation (Fig. S8(g) in the ESM).

We also investigated the effects of thickness on the mechanical response of the kirigami structure (Fig. S9 in the ESM). In stage III, as P1 bending is no longer the main deformation mechanism, a thickness effect is not observed. On the other hand, stages I and II are affected by a change in thickness. First, the transition strain at which the out-of-plane deformation initiates increases as the thickness increases (Figs. S9(a) and S9(b) in the ESM), which is consistent with the previous results [31]. In addition, the kirigami structures in stage II become stiffer as thickness (t) increases because the bending stiffness of the P1 plate increases with t^3.

From the above parametric study, we can derive an analytical equation that is capable of describing the σ_n–ε_n relation of the kirigami structure in stage II. At a certain nominal stress (σ_n), we can express the nominal strain (ε_n) of a kirigami structure given certain design parameters (g) and thickness, as $\delta_g(t,g)$, which is approximately given by the following equation

$$\delta_g(t,g) = c_1\delta_m/(1 + c_2t^2) \quad (2)$$

where c_1 and c_2 are constants and $\delta_m(g) = 18CH/L_T - 1$ (see Discussions in the ESM for the derivation). In the derivation, we assumed that the bendability of the P1 plate determines the overall stretchability of the kirigami structure. To confirm the validity of Eq. (2), we correlated $\delta_g(t,g)$ with FEA-simulated $\varepsilon_{10MPa}(t,g)$ of the kirigami structure by changing the various design parameters and t. Notably, $\varepsilon_{10MPa} \approx \delta_g$ with proper values of c_1 and c_2 (Fig. 3(f)). The resulting δ_g therefore enables a nearly analytical prediction of the stretchability for a kirigami structure with parameters g and thickness at a certain applied stress without requiring complex FEA simulations. In addition, the linear relation between ε_{10MPa} and δ_g further demonstrates that out-of-plane bending of P1 dominates overall deformation of kirigami structures.

To investigate the strain-insensitive electrical resistance of the patterned metal features (e.g., patterned Cr/Au/Ti temperature sensor in Fig. 1(c)) in our kirigami devices, we also simulated the strain of a line at the neutral plane (ε_L) of the kirigami bridge structure as a function of ε_n (Fig. S10(a) in the ESM). At $\varepsilon_n = 100\%$, ε_L is predicted to be 1.7%. The simulated ε_L is then converted to the change in electrical resistance using the equation with assumption that no cracks are formed in the electrode, $\Delta R/R_0 = (1 + \varepsilon_L)^2 - 1$(Fig. S10(b) in the ESM) [32]. As a result, $\Delta R/R_0$ is predicted to be 3.5% at $\varepsilon_n = 100\%$, which is higher than our experimental results. We attributed the difference between simulation and experimental results to formation of multiple microcracks or nanocracks in the electrodes during the fabrication processes. We confirmed these features by observing multiple microcracks and nanocracks (Fig. 3(g)) formed in Cr/Au thin film deposited on a polyimide kirigami structure. Such cracks may be formed during fabrication processes that induce unintentional mechanical deformation of the kirigami structure. When microcracks or nanocracks are formed, applied stresses are localized to the crack tips (Fig. 3(h)) [33]. This can lead to a significant reduction of strain in metal thin films (Fig. 3(i)). As a result, under small strains that do not induce additional crack propagation (< 5%), the change in electrical resistance of the cracked metal can be negligible [34].

It is worth noting here that the average strain in the neutral plane was predicted to be 60%–80% of the average strain in the top plane, which indicates that placing all electrodes in the middle of the polyimide film helps to achieve strain-insensitive electrical resistance (Fig. S11 in the ESM).

3.3 Solution-gated GFET-based sensors

As a demonstration of our kirigami devices for wearable sensor applications, we assessed the strain-insensitive sensor outputs by integrating the solution-gated graphene FETs in our kirigami-patterned mesh structures (Fig. 4(a)). Owing to their high conductivity, high surface area and robust chemical properties of graphene, solution-gated graphene transistors are considered one of the most promising bio/chemical sensors for quantifying analytes in solution using electrical signals. For the gate, an integrated planar gate electrode (Cr/Au/Ti) with thickness 15/150/15 nm was used. To measure the gate-modulated current of our GFETs, a droplet of phosphate-buffered saline (PBS), mimicking sweat, was placed on the island, thereby linking the integrated gate electrode to the three graphene channels through openings on the polyimide. The transfer curves of the GFETs were characterized by applying a varying gate voltage from 0 to 1.5 V during stretching. Our GFETs exhibited stable transfer curves during stretching. Furthermore, the Dirac voltage (V_{Dirac}) changed by less than 2% at applied strains between $\varepsilon_n = 0\%$ and $\varepsilon_n = 100\%$, and the

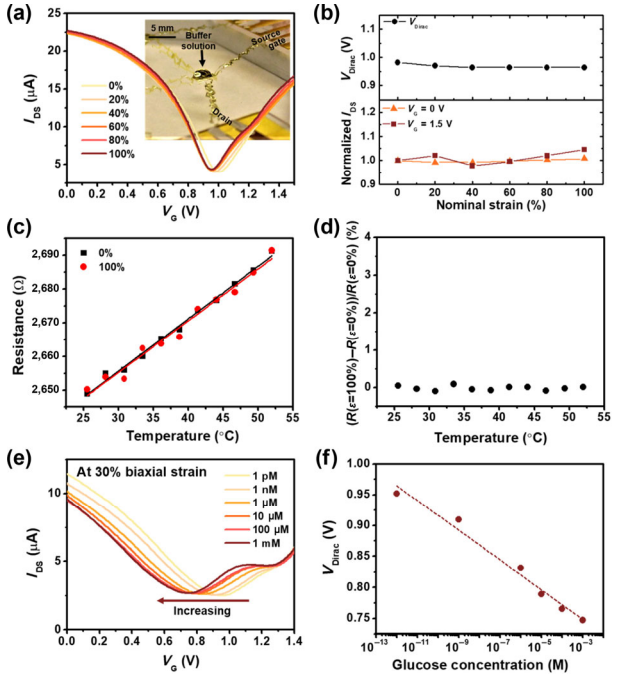

Figure 4 (a) Source-drain current (I_{DS}) versus of gate bias (V_G) of a solution-gated GFET at ε_n = 0%, 20%, 40%, 60%, 80%, 100%. Inset is a photograph of the experimental configuration with an island solution-gated GFET under stretching. (b) Dirac voltage (upper) and normalized I_{DS} at V_G = 0 V (triangle) and 1.5 V (square) (lower) as a function of ε_n. I_{DS} is normalized by I_{DS} at ε_n = 0%. (c) Resistance of temperature sensor as a function of temperature at ε_n = 0% (black square) and ε_n = 100% (red circle). (d) Normalized strain-dependent resistance change of the temperature sensor from ε_n = 0% to ε_n = 100% as a function of temperature. (e) I_{DS}–V_G curves of a GFET-based glucose sensor for different glucose concentrations. The measurement was carried out at ε_n = 30%. (f) Dirac voltage of the glucose sensor as a function of glucose concentration.

source-drain current (I_{DS}) at the gate voltage (V_G) of 0 and 1.5 V were also nearly independent of stretching (Fig. 4(b)). This stable operation of our GFETs clearly demonstrates that the graphene channel in the island remains intact during large degree of stretching. This compares favorably against conventional solution-gated GFETs fabricated on elastomers, which showed severe degradation due to the formation of microcracks when stretched more than 3% [35].

In addition, we also assessed the performance of a resistive temperature sensor on one of the islands from 25–55 °C at ε_n = 0% and ε_n = 100% (Fig. 4(c)). In the measured range, the resistance of the temperature sensor increased linearly with temperature as a result of enhanced electron–phonon scattering in the Cr/Au/Ti electrode. The sensitivity of the temperature sensor was 1.56 and 1.54 Ω/K at the neutral state and stretched state, respectively. The normalized resistance change between 100% and 0% stretching at each measured temperature was negligibly small (Fig. 4(d)), thereby showing strain insensitivity.

Lastly, we demonstrated a solution-gated GFET-based glucose sensor embedded in our kirigami-patterned mesh structure. For the detection of glucose, glucose oxidase (GO_x) was deposited on graphene channel surface. When glucose is oxidized by GO_x, gluconic acid and hydrogen peroxide (H_2O_2) are produced via following reaction [36]

$$\text{Glucose} + H_2O + O_2 \rightarrow \text{Gluconic acid} + H_2O_2 \quad (3)$$

GFET-based glucose sensors monitor the amount of H_2O_2 produced, which is equal to the amount of glucose consumed [37]. The electrochemical reaction of H_2O_2 at gate electrode, $H_2O_2 \rightarrow O_2 + 2H^+ + 2e^-$, modifies the voltage drop at an electrical double layer on gate/electrode interface. It changes

effective gate voltage that applies on the graphene channel, resulting in the shift in the Dirac voltage of the GFETs. At a biaxial strain of 30%, when glucose concentration decreased from 1 mM to 1 pM, a change in V_{Dirac} from 0.95 to 0.75 V was observed (Fig. 4(e)). The sensitivity of our glucose sensor with integrated gate electrode was −24 mV/decade in the glucose concentration range of 1 pM to 1 mM (Fig. 4(f)), consistent with previous results [38]. Since the reported glucose concentration in sweat for diabetic patients is between 0.01 and 1 mM [39], this shows that our glucose sensor can be used as wearable sweat sensor for non-invasive monitoring.

4 Conclusions

In conclusion, we demonstrated a biaxially-stretchable kirigami-patterned mesh platform for motion-artifact free, graphene-based wearable sensors. When graphene and metal electrodes were embedded in the structure, the change in their electrical resistance was less than ~ 0.5% under mechanical deformations such as 180° twisting and 100% biaxial stretching. Using FEA simulations, the deformation mechanism of the structure was investigated, revealing that out-of-plane deformation of kirigami bridges is a key factor that governs the stretchability of kirigami structures. In addition, we derived a simple equation that relates the stretchability of a kirigami structure with various design parameters. This equation gives insight into the deformation mechanisms of kirigami structures, and also enables prediction for the stretchability of future kirigami designs. Moreover, we demonstrated strain-insensitive performance of solution-gated GFETs, which offers promising potential for various bio-sensing applications. Lastly, we demonstrated strain-insensitive stretchable sensors that can monitor temperature and glucose concentration. Although our demonstration of kirigami devices is limited to sensing one signal at a time, we believe our kirigami devices can be integrated with electronic circuits for wearable healthcare systems that enable simultaneous monitoring of multiple bio-signals, data processing and data transmission.

Acknowledgements

S. N. gratefully acknowledges support from the AFOSR (Nos. FA2386-17-1-4071 and FA9550-18-1-0405), KRICT (No. GO!KRICT KK1963-807), NSF (Nos. ECCS-1935775, CMMI-1554019 and MRSEC DMR-1720633), NASA ECF (No. NNX16AR56G), ONR YIP (No. N00014-17-1-2830) and JITRI. Experiments were carried out in part in the Materials Research Laboratory Central Research Facilities, and Micro and Nano Technology Laboratory at the University of Illinois at Urbana–Champaign.

Electronic Supplementary Material: Supplementary material (including the fabrication scheme for the kirigami devices, the Raman spectrum of the graphene used, cross-sectional SEM images, additional FEA simulation results, and the derivation of Eq. (2)) is available in the online version of this article at https://doi.org/10.1007/s12274-020-2662-7.

Dedication

This article is dedicated to Charlie who taught me the pursuit of excellence and creativity in research. I was a member of Lieber group from 2005 to 2011, and received my PhD degree in Applied Physics at Harvard University under the supervision of Charlie in 2011. My memory of Charlie can be summed up in three parts: pioneer in nanoscience, generous mentor and supporter, and champion pumpkin grower! This photo of Charlie and I, and his academic grandchildren (Peter, Juyoung, Mike, Keong, and Jin Myung) was taken on April 21, 2018 when Charlie delivered the Krug Lecture at the University of Illinois at Urbana-Champaign.

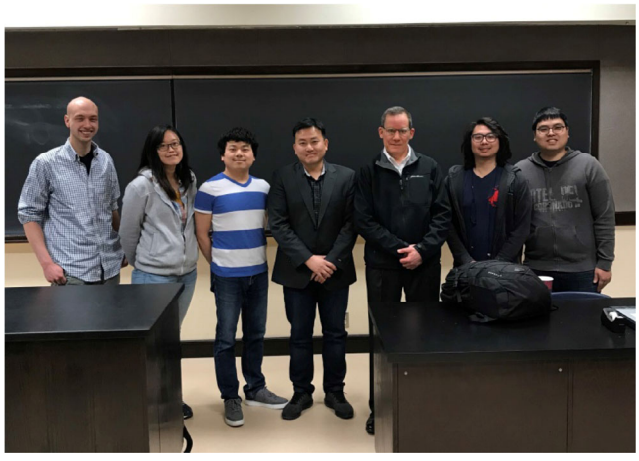

References

[1] Gao, W.; Emaminejad, S.; Nyein, H. Y. Y.; Challa, S.; Chen, K.; Peck, A.; Fahad, H. M.; Ota, H.; Shiraki, H.; Kiriya, D. et al. Fully integrated wearable sensor arrays for multiplexed *in situ* perspiration analysis. *Nature* **2016**, *529*, 509–514.

[2] Koh, A.; Kang, D.; Xue, Y. G.; Lee, S.; Pielak, R. M.; Kim, J.; Hwang, T.; Min, S.; Banks, A.; Bastien, P. et al. A soft, wearable microfluidic device for the capture, storage, and colorimetric sensing of sweat. *Sci. Transl. Med.* **2016**, *8*, 366ra165.

[3] Kim, J.; Campbell, A. S.; de Ávila, B. E. F.; Wang, J. Wearable biosensors for healthcare monitoring. *Nat. Biotechnol.* **2019**, *37*, 389–406.

[4] Lee, H.; Choi, T. K.; Lee, Y. B.; Cho, H. R.; Ghaffari, R.; Wang, L.; Choi, H. J.; Chung, T. D.; Lu, N. S.; Hyeon, T. et al. A graphene-based electrochemical device with thermoresponsive microneedles for diabetes monitoring and therapy. *Nat. Nanotechnol.* **2016**, *11*, 566–572.

[5] Jeong, J. W.; Yeo, W. H.; Akhtar, A.; Norton, J. J. S.; Kwack, Y. J.; Li, S.; Jung, S. Y.; Su, Y. W.; Lee, W.; Xia, J. et al. Materials and optimized designs for human-machine interfaces via epidermal electronics. *Adv. Mater.* **2013**, *25*, 6839–6846.

[6] Bariya, M.; Nyein, H. Y. Y.; Javey, A. Wearable sweat sensors. *Nat. Electron.* **2018**, *1*, 160–171.

[7] Yamada, T.; Hayamizu, Y.; Yamamoto, Y.; Yomogida, Y.; Izadi-Najafabadi, A.; Futaba, D. N.; Hata, K. A stretchable carbon nanotube strain sensor for human-motion detection. *Nat. Nanotechnol.* **2011**, *6*, 296–301.

[8] Kim, D. H.; Lu, N. S.; Ma, R.; Kim, Y. S.; Kim, R. H.; Wang, S. D.; Wu, J.; Won, S. M.; Tao, H.; Islam, A. et al. Epidermal electronics. *Science* **2011**, *333*, 838–843.

[9] Kim, D. H.; Song, J. Z.; Choi, W. M.; Kim, H. S.; Kim, R. H.; Liu, Z. J.; Huang, Y. Y.; Hwang, K. C.; Zhang, Y. W.; Rogers, J. A. Materials and noncoplanar mesh designs for integrated circuits with linear elastic responses to extreme mechanical deformations. *Proc. Natl. Acad. Sci. USA* **2008**, *105*, 18675–18680.

[10] Miyamoto, A.; Lee, S.; Cooray, N. F.; Lee, S.; Mori, M.; Matsuhisa, N.; Jin, H.; Yoda, L.; Yokota, T.; Itoh, A. et al. Inflammation-free, gas-permeable, lightweight, stretchable on-skin electronics with nanomeshes. *Nat. Nanotechnol.* **2017**, *12*, 907–913.

[11] Tian, B. Z.; Liu, J.; Dvir, T.; Jin, L. H.; Tsui, J. H.; Qing, Q.; Suo, Z. G.; Langer, R.; Kohane, D. S.; Lieber, C. M. Macroporous nanowire nanoelectronic scaffolds for synthetic tissues. *Nat. Mater.* **2012**, *11*, 986–994.

[12] Hong, G. S.; Fu, T. M.; Qiao, M.; Viveros, R. D.; Yang, X.; Zhou, T.; Lee, J. M.; Park, H. G.; Sanes, J. R.; Lieber, C. M. A method for single-neuron chronic recording from the retina in awake mice. *Science* **2018**, *360*, 1447–1451.

[13] Liu, J.; Fu, T. M.; Cheng, Z. G.; Hong, G. S.; Zhou, T.; Jin, L. H.; Duvvuri, M.; Jiang, Z.; Kruskal, P.; Xie, C. et al. Syringe-injectable electronics. *Nat. Nanotechnol.* **2015**, *10*, 629–636.

[14] Kim, D. H.; Viventi, J.; Amsden, J. J.; Xiao, J. L.; Vigeland, L.; Kim, Y. S.; Blanco, J. A.; Panilaitis, B.; Frechette, E. S.; Contreras, D. et al. Dissolvable films of silk fibroin for ultrathin conformal bio-integrated electronics. *Nat. Mater.* **2010**, *9*, 511–517.

[15] Fu, T. M.; Hong, G. S.; Viveros, R. D.; Zhou, T.; Lieber, C. M. Highly scalable multichannel mesh electronics for stable chronic brain electrophysiology. *Proc. Natl. Acad. Sci. USA* **2017**, *114*, E10046–E10055.

[16] Blees, M. K.; Barnard, A. W.; Rose, P. A.; Roberts, S. P.; McGill, K. L.; Huang, P. Y.; Ruyack, A. R.; Kevek, J. W.; Kobrin, B.; Muller, D. A. et al. Graphene kirigami. *Nature* **2015**, *524*, 204–207.

[17] Song, Z. M.; Wang, X.; Lv, C.; An, Y. H.; Liang, M. B.; Ma, T.; He, D.; Zheng, Y. J.; Huang, S. Q.; Yu, H. Y. et al. Kirigami-based stretchable lithium-ion batteries. *Sci. Rep.* **2015**, *5*, 10988.

[18] Lamoureux, A.; Lee, K.; Shlian, M.; Forrest, S. R.; Shtein, M. Dynamic kirigami structures for integrated solar tracking. *Nat. Commun.* **2015**, *6*, 8092.

[19] Won, P.; Park, J. J.; Lee, T.; Ha, I.; Han, S.; Choi, M.; Lee, J.; Hong, S.; Cho, K. J.; Ko, S. H. Stretchable and transparent kirigami conductor of nanowire percolation network for electronic skin applications. *Nano Lett.* **2019**, *19*, 6087–6096.

[20] Tang, Y. C.; Lin, G. J.; Yang, S.; Yi, Y. K.; Kamien, R. D.; Yin, J. Programmable kiri-kirigami metamaterials. *Adv. Mater.* **2017**, *29*, 1604262.

[21] Shyu, T. C.; Damasceno, P. F.; Dodd, P. M.; Lamoureux, A.; Xu, L. Z.; Shlian, M.; Shtein, M.; Glotzer, S. C.; Kotov, N. A. A kirigami approach to engineering elasticity in nanocomposites through patterned defects. *Nat. Mater.* **2015**, *14*, 785–789.

[22] Morikawa, Y.; Yamagiwa, S.; Sawahata, H.; Numano, R.; Koida, K.; Ishida, M.; Kawano, T. Ultrastretchable kirigami bioprobes. *Adv. Healthc. Mater.* **2018**, *7*, 1701100.

[23] Xu, R. X.; Zverev, A.; Hung, A.; Shen, C. W.; Irie, L.; Ding, G.; Whitmeyer, M.; Ren, L. J.; Griffin, B.; Melcher, J. et al. Kirigami-inspired, highly stretchable micro-supercapacitor patches fabricated by laser conversion and cutting. *Microsyst. Nanoeng.* **2018**, *4*, 36.

[24] Novoselov, K. S.; Fal'ko, V. I.; Colombo, L.; Gellert, P. R.; Schwab, M. G.; Kim, K. A roadmap for graphene. *Nature* **2012**, *490*, 192–200.

[25] Akinwande, D.; Petrone, N.; Hone, J. Two-dimensional flexible nanoelectronics. *Nat. Commun.* **2014**, *5*, 5678.

[26] Lee, C.; Wei, X. D.; Kysar, J. W.; Hone, J. Measurement of the elastic properties and intrinsic strength of monolayer graphene. *Science* **2008**, *321*, 385–388.

[27] Chung, C.; Kim, Y. K.; Shin, D.; Ryoo, S. R.; Hong, B. H.; Min, D. H. Biomedical applications of graphene and graphene oxide. *Acc. Chem. Res.* **2013**, *46*, 2211–2224.

[28] Snapp, P.; Kang, P.; Leem, J.; Nam, S. Colloidal photonic crystal strain sensor integrated with deformable graphene phototransducer. *Adv. Funct. Mater.* **2019**, *29*, 1902216.

[29] Kang, P.; Wang, M. C.; Knapp, P. M.; Nam, S. Crumpled graphene photodetector with enhanced, strain-tunable, and wavelength-selective photoresponsivity. *Adv. Mater.* **2016**, *28*, 4639–4645.

[30] Yong, K.; De, S.; Hsieh, E. Y.; Leem, J.; Aluru, N. R.; Nam, S. W. Kirigami-inspired strain-insensitive sensors based on atomically-thin materials. *Mater. Today*, in press, DOI: 10.1016/j.mattod.2019.08.013.

[31] Isobe, M.; Okumura, K. Initial rigid response and softening transition of highly stretchable kirigami sheet materials. *Sci. Rep.* **2016**, *6*, 24758.

[32] Lu, N. S.; Wang, X.; Suo, Z. G.; Vlassak, J. Metal films on polymer substrates stretched beyond 50%. *Appl. Phys. Lett.* **2007**, *91*, 221909.

[33] Matsuhisa, N.; Jiang, Y.; Liu, Z. Y.; Chen, G.; Wan, C. J.; Kim, Y.; Kang, J.; Tran, H.; Wu, H. C.; You, I. et al. High-transconductance stretchable transistors achieved by controlled gold microcrack morphology. *Adv. Electron. Mater.* **2019**, *5*, 1900347.

[34] Cao, W. Z.; Görrn, P.; Wagner, S. Modeling the electrical resistance of gold film conductors on uniaxially stretched elastomeric substrates. *Appl. Phys. Lett.* **2011**, *98*, 212112.

[35] Lee, S. K.; Kim, B. J.; Jang, H.; Yoon, S. C.; Lee, C.; Hong, B. H.; Rogers, J. A.; Cho, J. H.; Ahn, J. H. Stretchable graphene transistors with printed dielectrics and gate electrodes. *Nano Lett.* **2011**, *11*, 4642–4646.

[36] Heller, A.; Feldman, B. Electrochemical glucose sensors and their applications in diabetes management. *Chem. Rev.* **2008**, *108*, 2482–2505.

[37] Huang, Y. X.; Dong, X. C.; Shi, Y. M.; Li, C. M.; Li, L. J.; Chen, P. Nanoelectronic biosensors based on CVD grown graphene. *Nanoscale* **2010**, *2*, 1485–1488.

[38] Zhang, M.; Liao, C. Z.; Mak, C. H.; You, P.; Mak, C. L.; Yan, F. Highly sensitive glucose sensors based on enzyme-modified whole-graphene solution-gated transistors. *Sci. Rep.* **2015**, *5*, 8311.

[39] Lee, H.; Song, C.; Hong, Y. S.; Kim, M. S.; Cho, H. R.; Kang, T.; Shin, K.; Choi, S. H.; Hyeon, T.; Kim, D. H. Wearable/disposable sweat-based glucose monitoring device with multistage transdermal drug delivery module. *Sci. Adv.* **2017**, *3*, e1601314.